First-principles equation of state of polystyrene and its effect on inertial confinement fusion implosions

S. X. Hu (□□□), L. A. Collins, V. N. Goncharov, J. D. Kress, R. L. McCrory, and S. Skupsky

Phys. Rev. E **92**, 043104 — Published 14 October 2015

DOI: 10.1103/PhysRevE.92.043104

First-Principles Equation of State of Polystyrene (CH) and Its Effect on Inertial Confinement Fusion Implosions

S. X. Hu(胡素兴)[1,*], L. A. Collins[2], V. N. Goncharov[1], J. D. Kress[2], R. L. McCrory[1,+]

and S. Skupsky[1]

[1]Laboratory for Laser Energetics, University of Rochester

250 East River Road, Rochester, NY 14623-1299

[2]Theoretical Division, Los Alamos National Laboratory, Los Alamos, NM 87545

[*]E-mail: shu@lle.rochester.edu

[+]also at Department of Physics and Astronomy and Department of Mechanical Engineering, University of Rochester

Abstract

Obtaining an accurate equation of state (EOS) of polystyrene (CH) is crucial to reliably design inertial confinement fusion (ICF) capsules using CH/CH-based ablators. With first-principles calculations, we have investigated the extended EOS of CH over a wide range of plasma conditions (ρ = 0.1 to 100 g/cm^3 and T = 1,000 to 4,000,000 K). When compared with the widely used *SESAME*-EOS table, the first-principles equation of state (FPEOS) of CH has shown significant differences in the low-temperature regime, in which strong coupling and electron degeneracy play an essential role in determining plasma properties. Hydrodynamic simulations of cryogenic target implosions on OMEGA using the FPEOS table of CH have predicted ~30% decrease in neutron yield in comparison with the usual *SESAME* simulations. This is attributed to the ~5% reduction in implosion velocity that is caused by the ~10% lower mass ablation rate of CH predicted by FPEOS. Simulations using CH-FPEOS show better agreement with measurements of Hugoniot temperature and scattered light from ICF implosions.

PACS numbers: 52.27. Gr, 51.30. ti, 64.30. –t, 52.57.

I. INTRODUCTION

Controlled inertial confinement fusion (ICF)[1] has been pursued in laboratories for decades as a possibly viable route to clean energy. Materials involved in ICF target implosions undergo extreme plasma conditions such as warm dense matter (WDM) of temperatures from a few to several hundreds of electron volts and densities from 10^{21} to 10^{25} ions/cm^3. Properties of materials in this critical WDM regime have received much attention because of the wide existence of such extreme conditions in the interiors of giant/exoplanets,[2] the atmospheres of stars,[3] and laser-produced plasmas,[4] in addition to ICF capsules. Precisely determining the properties of WDM has proved challenging since the strong coupling and quantum effects play a critical role in these complex systems. High-energy-density (HED) experiments,[5–7] equipped with accurate diagnostic tools such as x-ray Thomson scattering[8–10] and x-ray absorption spectroscopy,[11,12] have begun to provide detailed tests of various theoretical models of WDM.

For ICF capsules consisting of a cryogenic deuterium–tritium (DT) shell covered by an ablator layer, accurate knowledge of the material properties would advance the understanding of target performance, thereby leading to more reliable ICF target designs.[13] The microphysics responsible for the static, dynamical, and optical properties of DT and ablators determines not only the shock strength and timing,[14,15] but also ionization stages,[16] thermal conduction,[17] and nonuniformity growth[18] in ICF implosions. In particular, the equation of state (EOS) of DT and ablators is essential to closing the hydrodynamic equations for ICF simulations and to determine the material compressibility[19] and the mass ablation rate,[20] which in turn control the implosion velocity and the growth of Rayleigh–Taylor instability.[18] In addition, an accurate EOS of ablators can lead to better predictions of the blowoff plasma conditions, which helps tighten the laser–plasma interaction models used in integrated ICF simulations. Precisely determining the EOS of materials under such HED conditions has remained elusive in the past because of the complexity. A variety of physics models were adopted to compute the EOS of materials. For example, the original *SESAME*-EOS library[21] was based on the free-energy model of matter, while the quotidian equation of state (QEOS)[22] was derived from the improved Thomas–Fermi model. The *SESAME* model used a Helmholtz free energy consisting of a cold curve, an ion thermal contribution, and thermal excitation of electrons calculated by the Thomas–Fermi–Dirac average-atom model. Although such global EOS models have been useful and widely used in the past, their accuracy is worth re-examining in order to make reliable ICF designs and to constrain laser–plasma interaction model, since the margin for ignition is typically small.

Hydrocarbon polymers, such as polystyrene (CH), are often chosen as ablators in both indirect-drive[23–25] and direct-drive[26–28] ICF targets because they are inexpensive and easy to make. Upon laser or x-ray irradiation, CH can be shocked to high pressures from Mbar to Gbar. Depending on the driving laser/x-ray pulse shape, the shocked CH may also relax to a temperature well below ~5 eV at near-solid densities. Just as important as the properties of the DT fuel[29–45] are to ICF implosions, accurate knowledge of the CH ablator in the WDM regime is also crucial for reliable ICF designs. Thanks to advances of first-principles methods, studies of plasma properties under HED conditions have become possible in recent years. These first-principles investigations have covered the static EOS of a variety of materials including hydrogen/deuterium,[29–45] carbon,[46] polystyrene,[47–50] and polyethylene;[51] as well as the transport and optical properties of hydrogen/deuterium[17,52–57] in the WDM regime.

In contrast to previous EOS studies of CH in limited ranges of densities and temperatures along the principal Hugoniot[50], we have combined the two first-principles methods—the Kohn–Sham density-functional-theory–based molecular dynamics (KSMD) method[58,59] and the orbital-free molecular dynamics (OFMD) method[60]—to investigate the global EOS of CH in a wide range of plasma conditions. In this article, we report on the widely-ranged first-principles EOS (FPEOS) table of CH and its comparisons with both experiments and the *SESAME* model (table 7593 is used for CH) that is currently used in our hydrocodes. In particular, we illustrate the importance of an accurate CH ablator EOS to understand the 1-D physics of ICF implosions, through radiation–hydrodynamic simulations. The paper is arranged in the following: we first give a brief description of the two ab initio methods of KSMD and OFMD in Sec. II. Then, the FPEOS results and their comparisons with the *SESAME-EOS* model are made in Sec. III. In section IV, we present the FPEOS effect on ICF implosions through hydro-simulations. Finally, the paper is concluded in Sec. V.

II. THE *AB-INITIO* METHODS OF KSMD AND OFMD

The KSMD method has been implemented in the Vienna *ab-initio* simulation package (VASP),[61–63] which is based on the finite-temperature Kohn-Sham density-functional theory. In the KSMD calculations, the constant particle/volume/temperature ensemble is used, in which the electrons are described by quantum mechanics in plane wave basis within the generalized gradient approximation (GGA). The Perdew–Burke–Ernzerhof (PBE) exchange-correlation functional[64] was used in our KSMD calculations. The projector augmented wave (PAW) pseudopotentials were used to account for the core electrons. The PAW method is a generalization of the pseudopotential and linear augmented plane-wave methods, which allows efficient DFT calculations. To converge the energy and pressure calculations, we set the plane-wave cutoff energy to 1000 eV and adopted hard potentials with tight cores (core radii of 1.1 and 0.8 atomic units for C and H, respectively). The system was assumed to be in local thermodynamical equilibrium with equal electron and ion temperatures ($T_e = T_i$). A periodically replicated cubic cell was used with 125 or 216 atoms for each species of H and C, with the volume of the cell determined by the CH density. For each molecular dynamics (MD) step, a set of electronic state functions for each k point is self-consistently determined for a given ionic configuration. Then, the ions were moved classically with a velocity Verlet algorithm, according to the combined ionic force and the electronic force in the sense of Born-Oppenheimer approximation. The ion temperature was kept constant by simple velocity scaling. The KSMD calculations employed the Γ-point ($\mathbf{k} = 0$) sampling of the first

Brillouin zone in the cubic cell. We have tested with a 2 × 2 × 2 Monkhorst–Pack *k*-point grid and found the resulting pressure and energy varying only ~2%. For the lowest temperature point, we used 650 bands and a time step of $\Delta t = 0.5$ fs, while for the highest temperature points we employed a larger number (9000) of bands and a small time step of $\Delta t = 0.025$ fs. The KSMD calculations cover plasma temperatures from the low-T limit of T=1000 K up to the Fermi temperature (T_F) for each density point.

For high-temperature plasma conditions ($T > T_F$), we switched to the orbital-free molecular-dynamics (OFMD) method.[60] In the OFMD method, the electronic free energy is approximated by a direct functional of the electronic density through a semiclassical expansion of the Mermin functional. The leading and next-to-leading order expansions give the well-known finite-temperature Thomas-Fermi model. In order to preserve the electronic density beyond the cut-off radius, the OFMD method has introduced a norm-conserving regularization by imposing an analytical form to the electronic density within the cutoff volume. The electron exchange correlation functional is in the local-density approximation (LDA) for the OFMD simulations. The time steps used in our OFMD calculations vary from $2.4\text{x}10^{-2}$ fs to $4.8\text{x}10^{-3}$ fs, depending on the density and temperature of CH plasmas. The pressures calculated from both KSMD and OFMD methods at the boundary of $T \approx T_F$ are matched well within <1%.

III. COMPARISONS OF *FPEOS* WITH *SESAME* AND EXPERIMENTS

The FPEOS table of CH has been constructed from the KSMD–OFMD calculations for a wide range of densities of $\rho = 0.1$ to 100 g/cm^3 and temperatures of $T =$

1,000 to 4,000,000 K. The KSMD calculations cover all densities except $\rho = 0.1$ g/cm^3 for plasma temperatures up to T_F, while the OFMD computes higher-temperature and lower-density conditions. These FPEOS data fully cover the plasma conditions of an ablating CH shell. A supercell containing 250 to 432 atoms (C:H = 1:1) with periodic boundary conditions was used. To make the KSMD–OFMD results into a global EOS table for wide HED applications, we also used OFMD calculations to guide the linear extrapolation of the FPEOS data to both low-density and high-temperature points outside the direct calculations. Finally, the global FPEOS table of CH, given in Ref. [65], was implemented into the hydrocode *LILAC* for ICF implosion simulations.

Before we present its impact on ICF simulations, the FPEOS of CH is first compared with experiments and the *SESAME*-EOS model. In Fig. 1, we have plotted the principal Hugoniot predicted by our KSMD–OFMD calculations with solid lines. The KSMD predictions are made to ~60 Mbar, while the OFMD calculations take over and extend up to the high pressure of $P \approx 5$ Gbar. The Hugoniot matching at around $P \sim 20$ to 30 Mbar from the two first-principles (FP) calculations has been done with the "boot-strapping" technique.[66] This technique uses the Hugoniot matching to infer the internal energy E_0 of initial solid CH at room temperature for the OFMD dataset. As seen in Fig. 1(a), the global Hugoniot predicted from the KSMD–OFMD calculations smoothly extends from a low pressure of ~0.2 Mbar to 5 Gbar. The OFMD matchings at both T = 120,000 K and T = 220,000 K give almost identical Hugoniot predictions at high pressures. It is noted that we have avoided using the highest KSMD point for the OFMD-matching calculation, as the KSMD calculation at this highest temperature T=400,000-K is less accurate even though a large number (~12000) of energy bands was used. In comparison with the widely used *SESAME*-EOS model (Table 7593), the FP calculations predict CH being slightly stiffer in the pressure range of 5 to 80 Mbar, but softer in higher pressures up to ~5 Gbar. The maximum compression has been shifted from the *SESAME*-predicted $\rho_m = 4.55$ g/cm^3 at $P = 220$ Mbar to $\rho_m = 4.68$ g/cm^3 at $P = 440$ Mbar in the FPEOS because of the lower temperature inferred from FPEOS [see the inset of Fig. 1(b)]. In experiments, the EOS of CH has been extensively studied using gas-gun and laser-driven shock waves. The gas-gun experiment[67] was typically in the low-pressure regime ($P < 1$ Mbar), while the laser experiments at the Nova[68] and Omega Laser Facilities[69] have recorded shock strengths up to ~40 Mbar. Other shock experiments[49,70,71] of the CH Hugoniot have explored the pressure range of $P < 5$ Mbar. The available experimental data have been compared with the FPEOS and *SESAME* predictions in Fig. 1(a). In the pressure range of $P < 10$ Mbar, both predictions are in good agreement with experiments (within the experimental error). However, the Hugoniot temperature measured in the recent OMEGA experiment[69] is in much better agreement with the FPEOS prediction [see Fig. 1(b)]. The *SESAME* model predicts a maximum of ~30% higher Hugoniot temperature. This is because the *SESAME* model underestimates the internal energy in this pressure range (discussed in detail below). The stiffer behavior of CH, seen in the Nova experiment [e.g., Fig. 1(a)] at high pressures of $P = 10$ to 40 Mbar, seems to qualitatively point toward the FPEOS even though the experimental error bars were large.

Next, we examine the off-Hugoniot comparison between the FPEOS table and the *SESAME* model in Figs. 2 and 3, in which the total pressure (P), internal energy (E), and their variations are plotted as a function of CH density for different plasma temperatures.

Figures 2(a) and 2(c) display the direct comparisons of pressure and internal energy between FPEOS (solid lines) and *SESAME* (dashed lines) at $T = 15{,}625$ K (1.35 eV). At this low temperature, large differences in both P and E appear in the low-density regime of $\rho < 3$ g/cm^3. To clearly show the variations, we plot the percentage changes of P and E between FPEOS and *SESAME* in Figs. 2(b) and 2(d). The two panels indicate that the pressure variations can be as large as ~ –100% in the low-density regime ($\rho < 1.0$ g/cm^3), and the energy changes vary from +40% at $\rho = 0.5$ g/cm^3 to –20% at high densities. At such a low temperature and not too high densities, it is difficult for models to properly account for all of the important microscopic interactions among the variety of species (atoms, molecules, ions, and electrons) in warm dense plasmas. The first-principles methods take these interactions into account much completely, which is only limited by computational feasibility. When the CH plasma temperature increases to $T = 31{,}250$ K (≈2.7 eV) and $T = 125{,}000$ K (≈10.8 eV), the many-body and quantum effects become less dominant than in the low-T case. Therefore, the percentage variations between FPEOS and *SESAME*, shown in Fig. 3, are reduced as the plasma temperature increases. They change from ±20% at $T = 2.7$ eV to within ~±10% for the higher temperature of $T = 10.8$ eV [see Figs. 3(b) and 3(d)]. Although the DFT method may not treat the molecular dissociation accurately at lower densities, it is safe to say that for the warm-dense plasma conditions shown in Figs. 2 and 3 the molecular dissociation has been over [50]. Thus, the KSMD calculations should be trustable for these plasma conditions. Also it is evidenced in the comparison with experiments in Fig. 1(b), the FPEOS is indeed more accurate than the original *SESAME* model.

IV. THE IMPACT OF *FPEOS* ON ICF SIMULATIONS

With the FPEOS table of CH incorporated into *LILAC*, we can now simulate ICF implosions. The EOS for this initial CH condition has been extrapolated from our lowest temperature KSMD calculations. By comparing the hydrodynamic simulations using FPEOS with the *SESAME* simulations and experiments, we may examine how the more-accurate FPEOS of CH affects the 1-D predictions of target performance. As an example, we show the two hydro-simulation results in Figs. 4 and 5 for a cryogenic DT target implosion on OMEGA. Figure 4(a) plots the triple-picket pulse shape[72–74] with an inset of target dimensions. The cryo-DT target consists of a 49-μm DT layer with an 8.3-μm deuterated plastic (CD) ablator, which is imploded by the low-adiabat laser pulse. The EOS of CD was derived by mass-scaling of the CH-FPEOS. The 1-D hydro simulations for both cases have used the same nonlocal thermal-transport model[75] and cross-beam energy transfer model[76,77] in the laser absorption package. Upon the irradiation of the first laser picket, the plastic is ablated and a shock is launched into the shell. Figure 4(b) shows the density and temperature profiles as a function of target radius at t = 0.5 ns, in which the FPEOS results (solid lines) are compared to the *SESAME* simulation (dashed lines). At this time, the shock has transited into the DT layer and the plasma temperature in the CD shell is less than ~5 eV. The relaxation after the shock brings the CD density below the solid level (ρ_0 = 1.05 g/cm^3). This is the regime in which we found large differences (~±20% or more) between FPEOS and *SESAME*. As a result, the hydro simulation with FPEOS predicts a lower temperature in the shell (consistent with the lower temperature seen in the shock Hugoniot). This may lead to a smaller mass ablation rate of plastic in FPEOS. That is exactly what we saw in Fig. 4(c), where the FPEOS-predicted mass ablation rate is lower when compared with the *SESAME* simulation. As the "rocket" effect indicates, less mass ablation rate in FPEOS can lead to a smaller ablation pressure and a slower implosion velocity. We found that at the end of pulse (t = 2.5 ns) the FPEOS-predicted shell travels ~20 μm behind the *SESAME* simulation, and the ablation pressure is reduced by ~10%, from 92 Mbar (*SESAME*) to 83 Mbar with FPEOS. Furthermore, the slower ablation can affect the laser light scattering in the coronal plasma. Figure 4(d) displays the comparison of the two predictions with the scattered-light measurement on OMEGA [78]. The scattered light, which is the unabsorbed laser light during laser-target interaction, has been calculated in our hydrocode using the inverse-bremsstrahlung absorption and beam-to-beam energy-transfer models. It shows that the FPEOS simulation gives better agreement with experiment.

Finally, we discuss the overall target performance between the FPEOS and *SESAME* simulations. In Fig. 5(a) we plot the implosion velocities and neutron production rates as a function of time. Because of the smaller mass ablation rate of CH predicted by FPEOS [e.g., Fig. 4(c)], the implosion velocity is reduced by ~5%, varying from $V_{\text{imp}} \approx -3.7 \times 10^7$ m/s (*SESAME*) to $V_{\text{imp}} \approx -3.5 \times 10^7$ m/s (FPEOS). This causes a delay of ~50 ps in the neutron bang time (the time neutron rate reaches peak) for the FPEOS simulation. From the scaling law of $Y \propto V_{\text{imp}}^6$ for the neutron yield,[79–81] the ~5% reduction in V_{imp} can have a significant consequence in neutron production. Figure 5(a) shows a lower peak neutron rate in the FPEOS case (blue solid line), which gives a total neutron yield of $Y = 1.1 \times 10^{14}$ dropping from the *SESAME*-predicted value of $Y = 1.5 \times 10^{14}$. At their peak neutron production, Fig. 5(b) shows the hot-spot pressure and shell density degradation in the FPEOS simulation. The hot-spot peak pressure is reduced from P = 142 Gbar (*SESAME*) to P = 118 Gbar (FPEOS); and the DT shell is stagnated at slightly large radius and lower peak-density for the FPEOS simulation. Also, the neutron-averaged hot-spot temperature decreases from T_i = 3.6 keV (*SESAME*) to T_i = 3.4 keV (FPEOS), although the change in neutron-averaged $\langle \rho R \rangle$ is only moderate (<5%), $\langle \rho R \rangle$ = 262 mg/cm^2 (*SESAME*) versus $\langle \rho R \rangle$ = 250 mg/cm^2 (FPEOS).

V. CONCLUSION

In summary, we have combined the two *ab-initio* methods of KSMD and OFMD to calculate the equation of state for the ICF ablator material of CH, in a wide range of plasma conditions. Both the Hugoiniot's pressure and temperature, predicted from the FPEOS table, are in better agreement with experiments. Large differences in both pressure and energy have been observed in the low-temperature WDM regime when the FPEOS is compared with the widely used *SESAME* model. Hydro simulations of an ICF target implosion using the FPEOS of CH predict ~5% lower implosion velocity, ~10% decrease in ablation pressure, and ~30% neutron yield reduction relative to the usual *SESAME* simulation. These are caused by the smaller mass ablation rate predicted by the CH-FPEOS. The reduction of ablation velocity may have implications in nonuniformity growth at the ablation front, which will be examined in future multidimensional hydro simulations. Overall, the predicted scattered light with FPEOS simulation agrees better with experimental measurements. We hope that such an accurate FPEOS of ablators can be helpful for the reliable design of ICF targets and HEDP experiments.

Acknowledgment

This material is based upon work supported by the Department of Energy National Nuclear Security Administration under Award Number DE-NA0001944, the University of Rochester, and the New York State Energy Research and Development Authority. The support of DOE does not constitute an endorsement by DOE of the views expressed in this article. This work was also supported by Scientific Campaign 10 at the Los Alamos National Laboratory, operated by Los Alamos National Security, LLC for the National Nuclear Security Administration of the U.S. Department of Energy under Contract No. DE-AC52-06NA25396.

References

1. J. Nuckolls, L. Wood, A. Thiessen, and G. Zimmerman, Nature **239**, 139 (1972).
2. N. C. Santos, W. Benz, and M. Mayor, Science **310**, 251 (2005).
3. G. Fontaine, P. Brassard, and P. Bergeron, Publ. Astron. Soc. Pac. **113**, 409 (2001).
4. B. A. Hammel, S. W. Haan, D. S. Clark, M. J. Edwards, S. H. Langer, M. M. Marinak, M. V. Patel, J. D. Salmonson, and H. A. Scott, High Energy Density Phys. **6**, 171 (2010);

D. H. Froula, D. T. Michel, I. V. Igumenshchev, S. X. Hu, B. Yaakobi, J. F. Myatt, D. H. Edgell, R. Follett, V. Yu. Glebov, V. N. Goncharov *et al.*, Plasma Phys. Control. Fusion **54**, 124016 (2012).

5. S. H. Glenzer and R. Redmer, Rev. Mod. Phys. **81**, 1625 (2009).
6. S. H. Glenzer, B. J. MacGowan, P. Michel, N. B. Meezan, L. J. Suter, S. N. Dixit, J. L. Kline, G. A. Kyrala, D. K. Bradley, D. A. Callahan *et al.*, Science **327**, 1228 (2010).
7. A. L. Kritcher, T. Döppner, C. Fortmann, T. Ma, O. L. Landen, R. Wallace, and S. H. Glenzer, Phys. Rev. Lett. **107**, 015002 (2011).
8. S. H. Glenzer, G. Gregori, R. W. Lee, F. J. Rogers, S. W. Pollaine, and O. L. Landen, Phys. Rev. Lett. **90**, 175002 (2003).
9. B. Barbrel, M. Koenig, A. Benuzzi-Mounaix, E. Brambrink, C. R. D. Brown, D. O. Gericke, B. Nagler, M. Rabec le Gloahec, D. Riley, C. Spindloe *et al.*, Phys. Rev. Lett. **102**, 165004 (2009).
10. S. P. Regan, K. Falk, G. Gregori, P. B. Radha, S. X. Hu, T. R. Boehly, B. J. B. Crowley, S. H. Glenzer, O. L. Landen, D. O. Gericke *et al.*, Phys. Rev. Lett. **109**, 265003 (2012).
11. S. M. Vinko, O. Ciricosta, B. I. Cho, K. Engelhorn, H. K. Chung, C. R. D. Brown, T. Burian, J. Chalupsky, R. W. Falcone, C. Graves *et al.*, Nature **482**, 59 (2012).
12. O. Ciricosta, S. M. Vinko, H. K. Chung, B. I. Cho, C. R. D. Brown, T. Burian, J. Chalupský, K. Engelhorn, R. W. Falcone, C. Graves *et al.*, Phys. Rev. Lett. **109**, 065002 (2012).

13. S. X. Hu, V. N. Goncharov, T. R. Boehly, R. L. McCrory, S. Skupsky, L. A. Collins, J. D. Kress, and B. Militzer, Phys. Plasmas **22**, 056304 (2015).

14. T. R. Boehly, V. N. Goncharov, W. Seka, M. A. Barrios, P. M. Celliers, D. G. Hicks, G. W. Collins, S. X. Hu, J. A. Marozas, and D. D. Meyerhofer, Phys. Rev. Lett. **106**, 195005 (2011).

15. H. F. Robey, J. D. Moody, P. M. Celliers, J. S. Ross, J. Ralph, S. Le Pape, L. Berzak Hopkins, T. Parham, J. Sater, E. R. Mapoles *et al.*, Phys. Rev. Lett. **111**, 065003 (2013).

16. L. B. Fletcher, A. L. Kritcher, A. Pak, T. Ma, T. Döppner, C. Fortmann, L. Divol, O. S. Jones, O. L. Landen, H.□A. Scott *et al.*, Phys. Rev. Lett. **112**, 145004 (2014).

17. V. Recoules, F. Lambert, A. Decoster, B. Canaud, and J. Clérouin, Phys. Rev. Lett. **102**, 075002 (2009).

18. V. A. Smalyuk, D. T. Casey, D. S. Clark, M. J. Edwards, S. W. Haan, A. Hamza, D. E. Hoover, W. □W Hsing, O. Hurricane, J. □D Kilkenny *et al.*, Phys. Rev. Lett. **112**, 185003 (2014); V. A. Smalyuk, S. X. Hu, J. D. Hager, J. A. Delettrez, D. D. Meyerhofer, T. C. Sangster, and D. Shvarts, *ibid,* **103**, 105001 (2009).

19. S. X. Hu, V. A. Smalyuk, V. N. Goncharov, J. P. Knauer, P. B. Radha, I. V. Igumenshchev, J. A. Marozas, C. Stoeckl, B. Yaakobi, D. Shvarts *et al.*, Phys. Rev. Lett. **100**, 185003 (2008).

20. D. T. Michel, A. K. Davis, V. N. Goncharov, T. C. Sangster, S. X. Hu, I. V. Igumenshchev, D. D. Meyerhofer, W. Seka, and D. H. Froula, Phys. Rev. Lett. **114**, 155002 (2015).

21. B. I. Bennett, J. D. Johnson, G. I. Kerley, and G. T. Rood, Los Alamos National Laboratory, Los Alamos, NM, Report LA-7130 (1978).

22. R. M. More, K. H. Warren, D. A. Young, and G. B. Zimmerman, Phys. Fluids **31**, 3059 (1988).

23. S. W. Haan, J. D. Lindl, D. A. Callahan, D. S. Clark, J. D. Salmonson, B. A. Hammel, L. J. Atherton, R. C. Cook, M. J. Edwards, S. Glenzer *et al.*, Phys. Plasmas **18**, 051001 (2011).

24. M. J. Edwards, J. D. Lindl, B. K. Spears, S. V. Weber, L. J. Atherton, D. L. Bleuel, D. K. Bradley, D. A. Callahan, C. J. Cerjan, D. Clark *et al.*, Phys. Plasmas **18**, 051003 (2011).

25. C. Cherfils-Clérouin, C. Boniface, M. Bonnefille, P. Fremerye, D. Galmiche, P. Gauthier, J. Giorla, F. Lambert, S. Laffite, S. Liberatore *et al.*, J. Phys.: Conf. Ser. **244**, 022009 (2010).

26. D. D. Meyerhofer, R. L. McCrory, R. Betti, T. R. Boehly, D. T. Casey, T. J. B. Collins, R. S. Craxton, J. A. Delettrez, D. H. Edgell, R. Epstein *et al.*, Nucl. Fusion **51**, 053010 (2011).

27. R. L. McCrory, R. Betti, T. R. Boehly, D. T. Casey, T. J. B. Collins, R. S. Craxton, J. A. Delettrez, D. H. Edgell, R. Epstein, J. A. Frenje *et al.*, Nucl. Fusion **53**, 113021 (2013).

28. R. S. Craxton, K. S. Anderson, T. R. Boehly, V. N. Goncharov, D. R. Harding, J. P. Knauer, R. L. McCrory, P. W. McKenty, D. D. Meyerhofer, J. F. Myatt *et al.*, "Direct-Drive Inertial Confinement Fusion: A Review," to be published in Physics of Plasmas.

29. L. Caillabet, S. Mazevet, and P. Loubeyre, Phys. Rev. B **83**, 094101 (2011).

30. L. Caillabet, B. Canaud, G. Salin, S. Mazevet, and P. Loubeyre, Phys. Rev. Lett. **107**, 115004 (2011).

31. P. Loubeyre, S. Brygoo, J. Eggert, P. M. Celliers, D. K. Spaulding, J. R. Rygg, T. R. Boehly, G. W. Collins, and R. Jeanloz, Phys. Rev. B **86**, 144115 (2012).

32. S. X. Hu, B. Militzer, V. N. Goncharov, and S. Skupsky, Phys. Rev. Lett. **104**, 235003 (2010).

33. S. X. Hu, B. Militzer, V. N. Goncharov, and S. Skupsky, Phys. Rev. B **84**, 224109 (2011).

34. M. A. Morales, L. X. Benedict, D. S. Clark, E. Schwegler, I. Tamblyn, S. A. Bonev, A. A. Correa, and S. W. Haan, High Energy Density Phys. **8**, 5 (2012).

35. J. Vorberger, D. O. Gericke, and W. D. Kraeft, High Energy Density Phys. **9**, 448 (2013).

36. V. V. Karasiev, D. Chakraborty, O. A. Shukruto, and S. B. Trickey, Phys. Rev. B **88**, 161108(R) (2013).

37. C. Pierleoni, D. M. Ceperley, B. Bernu, and W. R. Magro, Phys. Rev. Lett. **73**, 2145 (1994).

38. B. Militzer and D. M. Ceperley, Phys. Rev. Lett. **85**, 1890 (2000).

39. J. Clérouin and J.-F. Dufrêche, Phys. Rev. E **64**, 066406 (2001).

40. L. A. Collins, S. R. Bickham, J. D. Kress, S. Mazevet, T. J. Lenosky, N. J. Troullier, and W. Windl, Phys. Rev. B **63**, 184110 (2001).

41. M. P. Desjarlais, Phys. Rev. B **68**, 064204 (2003).

42. B. Holst, R. Redmer, and M. P. Desjarlais, Phys. Rev. B **77**, 184201 (2008).

43. C. Wang and P. Zhang, Phys. Plasmas **20**, 092703 (2013).

44. A. Becker, W. Lorenzen, J. J. Fortney, N. Nettelmann, M. Schöttler, and R. Redmer, Astrophys. J. Suppl. Ser. **215**, 21 (2014).

45. L. X. Benedict, “A Review of Equation of State Models for Hydrogen,” to be published in World Scientific Review.

46. L. X. Benedict, K. P. Driver, S. Hamel, B. Militzer, T. Qi, A. A. Correa, A. Saul, and E. Schwegler, Phys. Rev. B **89**, 224109 (2014); R. F. Smith, J. H. Eggert, R. Jeanloz, T. S. Duffy, D. G. Braun, J. R. Patterson, R. E. Rudd, J. Biener, A. E. Lazicki, A. V. Hamza *et al.*, Nature **511**, 330 (2014).

47. C. Wang, X.-T. He, and P. Zhang, Phys. Plasmas **18**, 082707 (2011).

48. F. Lambert and V. Recoules, Phys. Rev. E **86**, 026405 (2012).

49. S. Hamel, L. X. Benedict, P. M. Celliers, M. A. Barrios, T. R. Boehly, G. W. Collins, T. Döppner, J. H. Eggert, D. R. Farley, D. G. Hicks *et al.*, Phys. Rev. B **86**, 094113 (2012).

50. S. X. Hu, T. R. Boehly, and L. A. Collins, Phys. Rev. E **89**, 063104 (2014).

51. T. R. Mattsson, J. M. D. Lane, K. R. Cochrane, M. P. Desjarlais, A. P. Thompson, F. Pierce, and G. S. Grest, Phys. Rev. B **81**, 054103 (2010).

52. B. Holst, M. French, and R. Redmer, Phys. Rev. B **83**, 235120 (2011).

53. F. Lambert, V. Recoules, A. Decoster, J. Clérouin, and M. Desjarlais, Phys. Plasmas **18**, 056306 (2011).

54. C. E. Starrett, J. Clérouin, V. Recoules, J. D. Kress, L. A. Collins, and D. E. Hanson, Phys. Plasmas **19**, 102709 (2012).

55. S. X. Hu, L. A. Collins, T. R. Boehly, J. D. Kress, V. N. Goncharov, and S. Skupsky, Phys. Rev. E **89**, 043105 (2014).

56. S. X. Hu, L. A. Collins, V. N. Goncharov, T. R. Boehly, R. Epstein, R. L. McCrory, and S. Skupsky, Phys. Rev. E **90**, 033111 (2014).

57. G. Faussurier and C. Blancard, Phys. Plasmas **22**, 042701 (2015).

58. L. Collins, I. Kwon, J. Kress, N. Troullier, and D. Lynch, Phys. Rev. E **52**, 6202 (1995).

59. J. G. Clérouin and S. Bernard, Phys. Rev. E **56**, 3534 (1997).

60. F. Lambert, J. Clérouin, and G. Zérah, Phys. Rev. E **73**, 016403 (2006).

61. G. Kresse and J. Hafner, Phys. Rev. B **47**, 558 (1993).

62. G. Kresse and J. Hafner, Phys. Rev. B **49**, 14251 (1994).

63. G. Kresse and J. Furthmüller, Phys. Rev. B **54**, 11169 (1996).

64. J. P. Perdew, K. Burke, and M. Ernzerhof, Phys. Rev. Lett. **77**, 3865 (1996); **78,** 1396 (1997)

65. See Supplemental Material at http://link.aps.org/supplemental/xxxxxx for the FPEOS table of CH.

66. D. Sheppard, J. D. Kress, S. Crockett, L. A. Collins, and M. P. Desjarlais, Phys. Rev. E **90**, 063314 (2014).

67. S. P. Marsh, ed. *LASL Shock Hugoniot Data*, Los Alamos Series on Dynamic Material Properties (University of California Press, Berkeley, CA, 1980).

68. R. Cauble, L. B. Da Silva, T. S. Perry, D. R. Bach, K. S. Budil, P. Celliers, G. W. Collins, A. Ng, T. W. Barbee, Jr., B. A. Hammel *et al.*, Phys. Plasmas **4**, 1857 (1997).

69. M. A. Barrios, D. G. Hicks, T. R. Boehly, D. E. Fratanduono, J. H. Eggert, P. M. Celliers, G. W. Collins, and D. D. Meyerhofer, Phys. Plasmas **17**, 056307 (2010).

70. M. Koenig, F. Philippe, A. Benuzzi-Mounaix, D. Batani, M. Tomasini, E. Henry, and T. Hall, Phys. Plasmas **10**, 3026 (2003).

71. N. Ozaki, T. Sano, M. Ikoma, K. Shigemori, T. Kimura, K. Miyanishi, T. Vinci, F. H. Ree, H. Azechi, T. Endo *et al.*, Phys. Plasmas **16**, 062702 (2009).

72. V. N. Goncharov, T. C. Sangster, T. R. Boehly, S. X. Hu, I. V. Igumenshchev, F. J. Marshall, R. L. McCrory, D. D. Meyerhofer, P. B. Radha, W. Seka *et al.*, Phys. Rev. Lett. **104**, 165001 (2010).

73. T. C. Sangster, V. N. Goncharov, R. Betti, P. B. Radha, T. R. Boehly, D. T. Casey, T. J. B. Collins, R. S. Craxton, J. A. Delettrez, D. H. Edgell *et al.*, Phys. Plasmas **20**, 056317 (2013).

74. S. X. Hu, V. N. Goncharov, P. B. Radha, J. A. Marozas, S. Skupsky, T. R. Boehly, T. C. Sangster, D. D. Meyerhofer, and R. L. McCrory, Phys. Plasmas **17**, 102706 (2010).

75. V. N. Goncharov, T. C. Sangster, P. B. Radha, R. Betti, T. R. Boehly, T. J. B. Collins, R. S. Craxton, J. A. Delettrez, R. Epstein, V. Yu. Glebov *et al.*, Phys. Plasmas **15**, 056310 (2008).

76. I. V. Igumenshchev, W. Seka, D. H. Edgell, D. T. Michel, D. H. Froula, V. N. Goncharov, R. S. Craxton, L. Divol, R. Epstein, R. Follett *et al.*, Phys. Plasmas **19**, 056314 (2012); D. H. Froula, T. J. Kessler, I. V. Igumenshchev, R. Betti, V. N. Goncharov, H. Huang, S. X. Hu, E. Hill, J. H. Kelly, D. D. Meyerhofer *et al.*, *ibid* **20**, 082704 (2013).

77. V. N. Goncharov, T. C. Sangster, R. Betti, T. R. Boehly, M. J. Bonino, T. J. B. Collins, R. S. Craxton, J. A. Delettrez, D. H. Edgell, R. Epstein *et al.*, Phys. Plasmas **21**, 056315 (2014).

78. W. Seka *et al.,* Phys. Plasms **15**, 056312 (2008).

79. M. C. Herrmann, M. Tabak, and J. D. Lindl, Nucl. Fusion **41**, 99 (2001).

80. C. D. Zhou and R. Betti, Phys. Plasmas **15**, 102707 (2008).

81. R. Nora, R. Betti, K. S. Anderson, A. Shvydky, A. Bose, K. M. Woo, A. R. Christopherson, J. A. Marozas, T. J. B. Collins, P. B. Radha *et al.*, Phys. Plasmas **21**, 056316 (2014).

Figure Captions

FIG. 1. (Color online) (a) The principal Hugoniot pressure is plotted as a function of shock density and (b) The temperature of Hugoniot versus pressure is shown. The Kohn–Sham DFT-based KSMD results (red circles) and the orbital-free molecular-dynamics (OFMD) predictions (red squares and green diamonds) are compared with the gas-gun experiment,[67] the Nova experiment,[68] and the recent impedance-matching experiment[69] on OMEGA. The prediction of *SESAME*-7593 is plotted with the dashed line.

FIG. 2. (Color online) The EOS comparisons of [(a) and (b)] pressure and [(c) and (d)] internal energy between FPEOS and *SESAME*-7593 as a function of CH density for a plasma temperature of $T \approx 1.35$ eV. (a) and (c) plot the actual values of pressure and energy, while (b) and (d) display the percentage variation between FPEOS and *SESAME*-7593.

FIG. 3. (Color online) Similar to Figs. 2(b) and 2(d) but for higher plasma temperatures of $T \approx 2.7$ eV and $T \approx 10.8$ eV. The variations between FPEOS and *SESAME*-7593 become smaller (toward the ~±10% range) as the plasma temperature increases.

FIG. 4. (Color online) The effect of CH-FPEOS on the cryogenic-DT target implosion on OMEGA: (a) the triple-picket pulse shape and target dimensions, (b) the density and temperature profiles at t = 0.5 ns that are predicted by radiation–hydrodynamic simulations using either FPEOS (solid lines) or *SESAME* (dashed lines) for the plastic

ablator, (c) the predicted mass ablation rates as a function of time, and (d) the comparison of scattered-light predictions with experimental measurement.

FIG. 5. (Color online) Comparisons of the implosion prediction between *SESAME*-EOS (dashed line) and FPEOS (solid line) of CH: (a) the implosion velocity and neutron production rate as a function of time and (b) the pressure and density as a function of target radius at the peak neutron production.

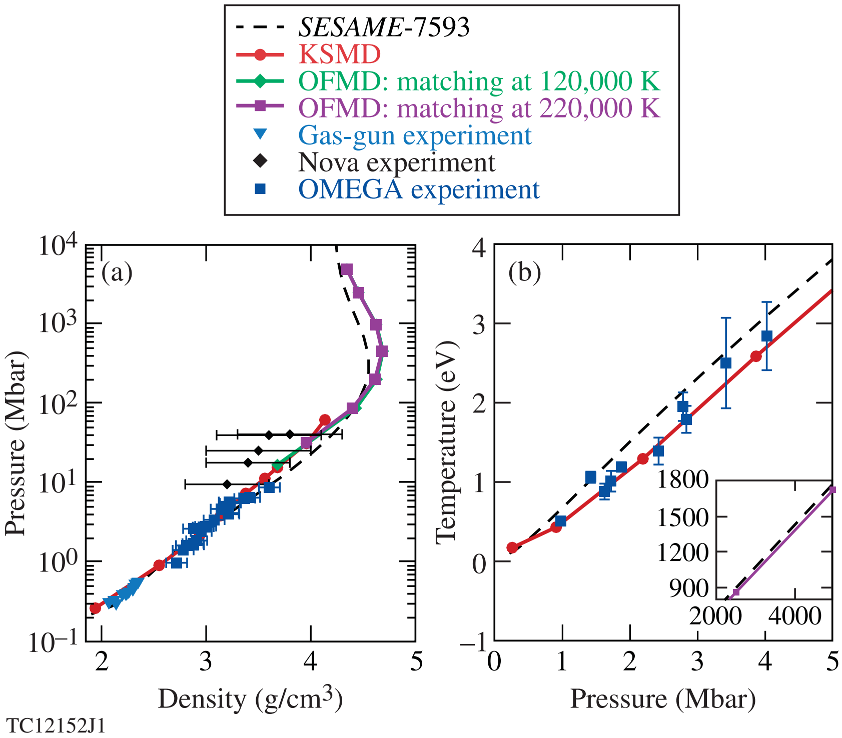

FIG. 1. (Color online) (a) The principal Hugoniot pressure is plotted as a function of shock density and (b) The temperature of Hugoniot versus pressure is shown. The Kohn–Sham DFT-based KSMD results (red circles) and the orbital-free molecular-dynamics (OFMD) predictions (red squares and green diamonds) are compared with the gas-gun experiment,[67] the Nova experiment,[68] and the recent impedance-matching experiment[69] on OMEGA. The prediction of *SESAME*-7593 is plotted with the dashed line.

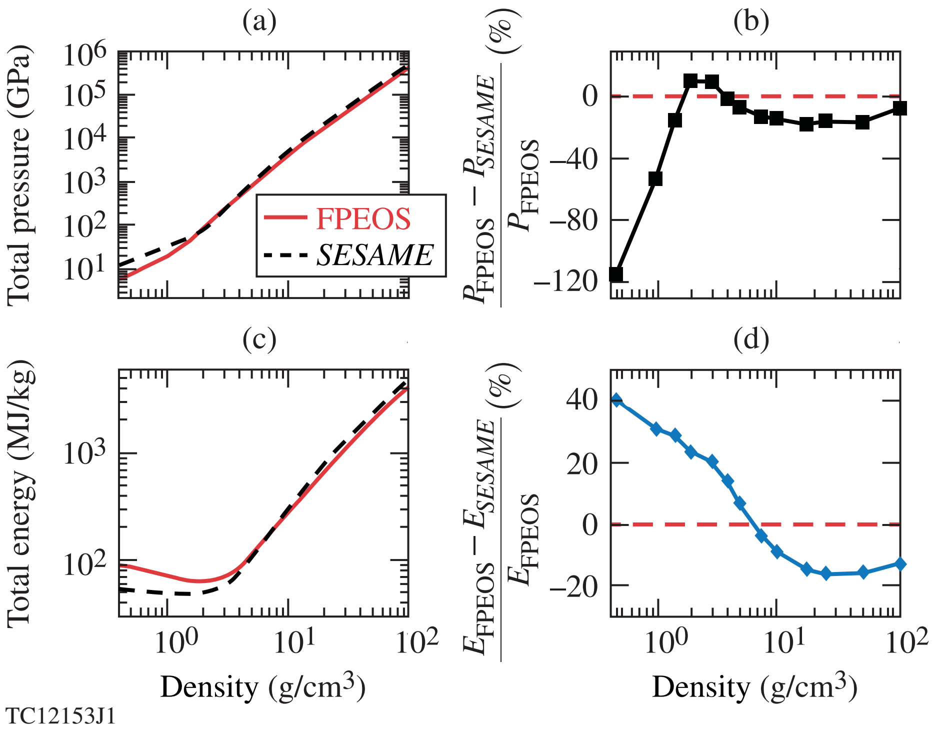

FIG. 2. (Color online) The EOS comparisons of [(a) and (b)] pressure and [(c) and (d)] internal energy between FPEOS and *SESAME*-7593 as a function of CH density for a plasma temperature of $T \approx 1.35$ eV. (a) and (c) plot the actual values of pressure and energy, while (b) and (d) display the percentage variation between FPEOS and *SESAME*-7593.

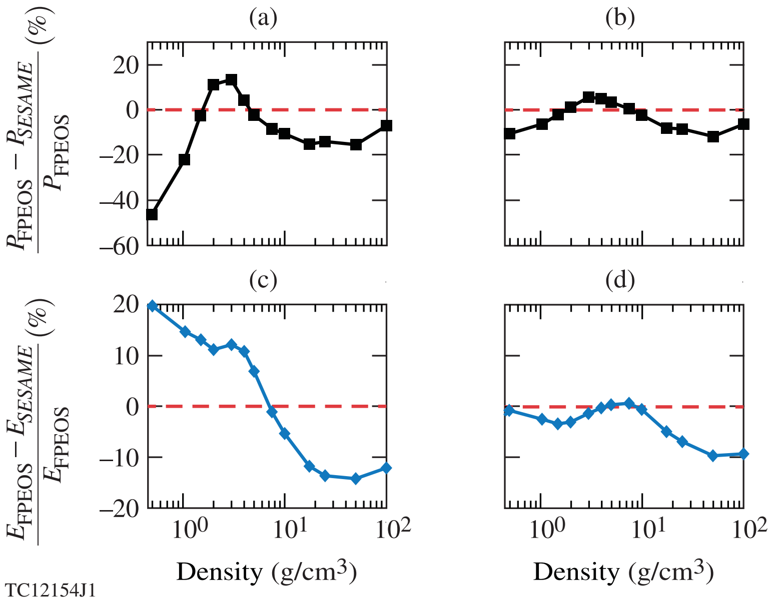

FIG. 3. (Color online) Similar to Figs. 2(b) and 2(d) but for higher plasma temperatures of $T \approx 2.7$ eV and $T \approx 10.8$ eV. The variations between FPEOS and *SESAME*-7593 become smaller (toward the ~±10% range) as the plasma temperature increases.

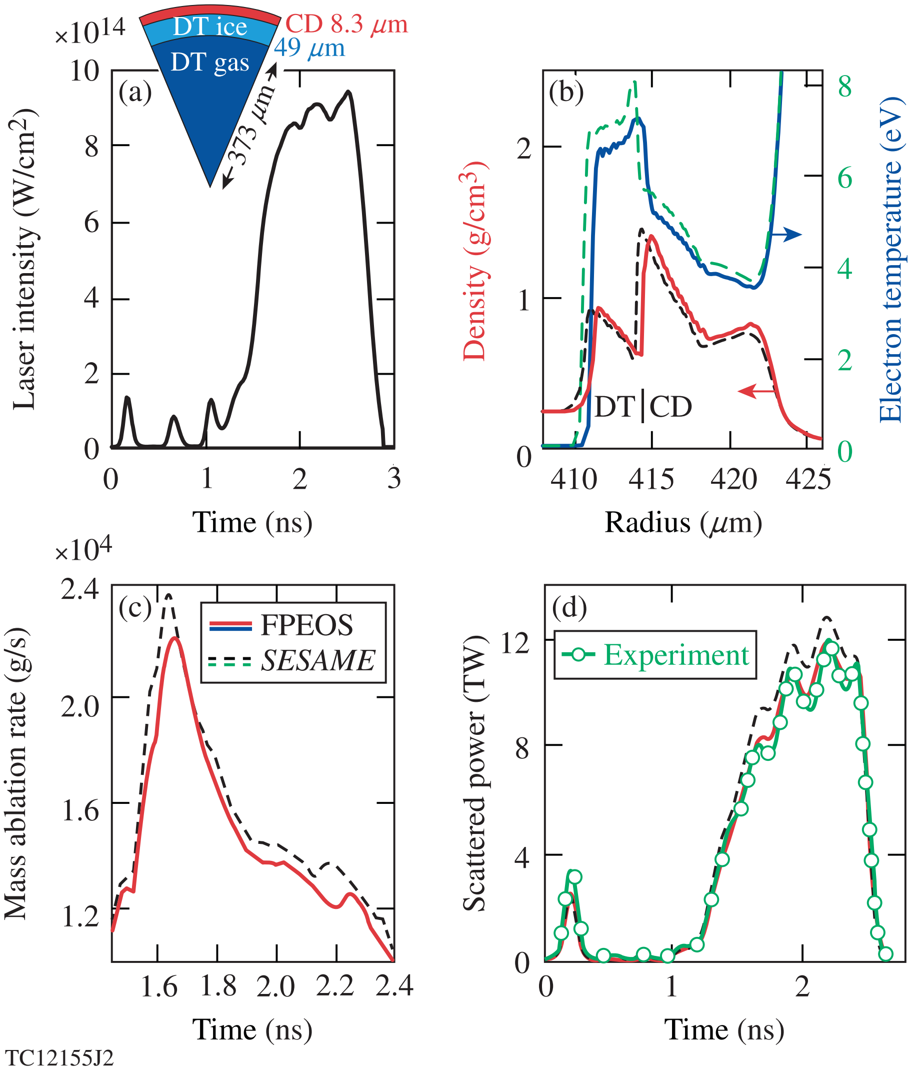

FIG. 4. (Color online) The effect of CH-FPEOS on the cryogenic-DT target implosion on OMEGA: (a) the triple-picket pulse shape and target dimensions, (b) the density and temperature profiles at t = 0.5 ns that are predicted by radiation–hydrodynamic simulations using either FPEOS (solid lines) or *SESAME* (dashed lines) for the plastic ablator, (c) the predicted mass ablation rates as a function of time, and (d) the comparison of scattered-light predictions with experimental measurement.

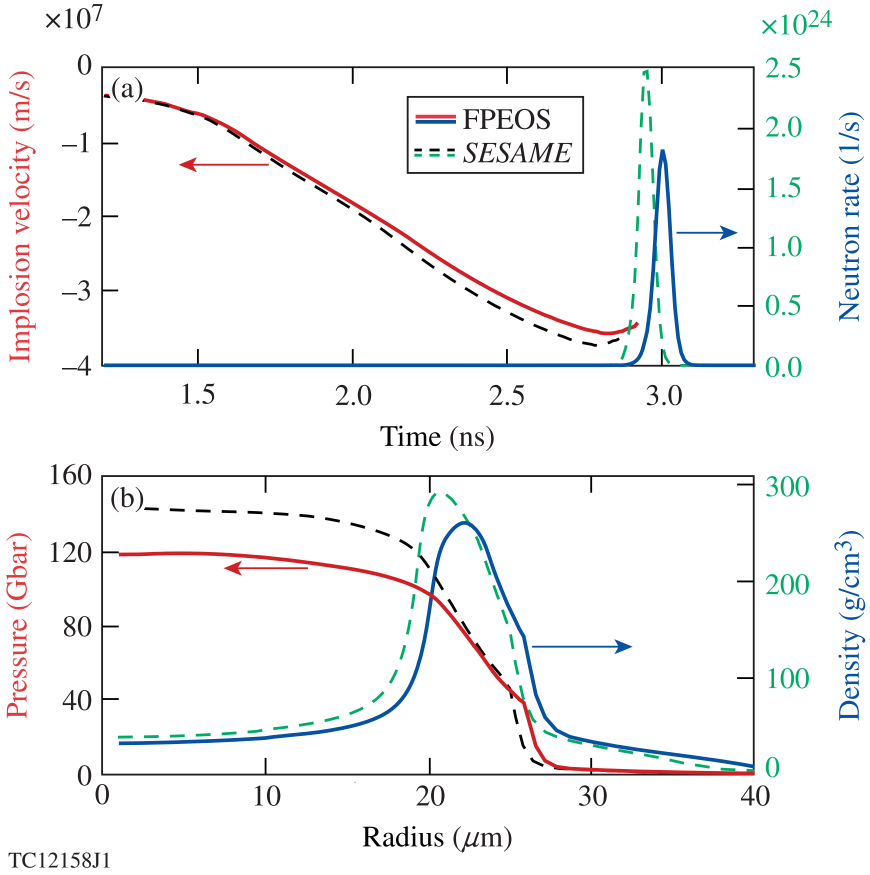

FIG. 5. (Color online) Comparisons of the implosion prediction between *SESAME*-EOS (dashed line) and FPEOS (solid line) of CH: (a) the implosion velocity and neutron production rate as a function of time and (b) the pressure and density as a function of target radius at the peak neutron production.